Transmission through multiple Mott insulator–semiconductor wells

Jan Verlage and Peter Kratzer
Fakultät für Physik and CENIDE, Universität Duisburg-Essen, Lotharstraße 1, 47057 Duisburg, Germany

(Received 28 February 2025; revised 12 May 2025; accepted 14 May 2025; published 27 May 2025)

Weakly and strongly interacting quantum many-body systems, namely semiconductors and Mott insulators, are combined into a layered heterostructure. Via the hierarchy of correlations, we derive and match the propagating quasiparticle solutions in the different regions and calculate the transmission coefficients through these layered structures. As a proof of principle, we find the well-known transmission bands of a semiconductor heterostructure. Extending this idea to semiconductor and Mott insulator structures we calculate the transmittance and the resonance energies. Within a phase accumulation model we find analytical expressions for the scattering phase shift. Lastly, we find transmission curves with skewness for structures with applied voltage.

DOI: 10.1103/PhysRevB.111.195158

I. INTRODUCTION

Superlattices, engineered structures composed of alternating layers of different materials, have emerged as fascinating platforms for exploring novel electronic and optical properties. Their ability to exhibit unique phenomena, such as quantum confinement [1–3] and collective behavior, has captivated researchers in various disciplines. Traditionally, superlattices have been engineered predominantly from materials with well-defined metallic or semiconducting characteristics [4–6], e.g., GaAs/$Al_xGa_{1-x}As$ [7,8]. Moreover, they show energy filtering over potential barriers [9–12]. This plays a crucial role in applications including thermoelectric devices, photovoltaics, or energy storage [13–15]. In the thermoelectric setting, a skewness of the transport distribution function is desired to simultaneously improve the different constituents, enhancing the thermoelectric power [16].

In contrast to semiconductor characteristics, Mott insulators [17,18] are a class of materials characterized by their unusual behavior that defies conventional band theory. Standard band theory describes them as conductors, but the insulating behaviorarises from strong electron-electron interactions that result in localized, rather than itinerant, electronic states [19,20]. Mott insulators have been the subject of intense investigation for several decades, due to their relevance to a range of phenomena, including, for example, high-temperature superconductivity [21,22]. In these materials, the transmission happens via quasiparticles showing distinct characteristics from usual semiconducting materials [23].

However, incorporating Mott insulators within the superlattice architecture, e.g., as ultrathin silicide layers in silicon [24,25], introduces an additional dimension of control through strong electron correlations. The strength of the Coulomb interaction between the electrons changes the size of the Mott gap. This effectively influences the transmission of electrons passing through these layers as doublon-holon quasiparticles. This allows for a better tailoring of the transmission characteristics compared to structures that lack this degree of freedom, and the Mott insulating layers introduce an additional skewness of the transmission favorable in thermoelectric applications.

One material class suitable for this heterostructure design is perovskites like TiF_3 [26] and $LaTiO_3$ [27], especially the interfaces $LaAlO_3/SrTiO_3$ [28,29], $LaAlO_3/SrTiO_3$ [30], $LaTiO_3/KTaO_3$ [27,31], or $LaTiO_3/SrTiO_3$ [32–34]. The correlation strength in these perovskites can be tuned by varying the central atom, and their interfaces can be grown with high precision. Alternatively, stacked heterostructures bound by van der Waals forces [35] facilitate the integration of various components such as single-band Mott insulators [36], the Mott insulating state of FeSe [37], or layered Mott insulating materials like $FePX_3$ (X = S, Se) [38], alongside semiconducting van der Waals materials.

Usually the Mott behavior is treated within a DMFT framework which takes the individual layers as infinite dimensional [39,40]. In this work, we use an approach via the hierarchy of correlations [41–43]. This method provides a powerful tool for describing both the weakly interacting semiconductors and strongly interacting Mott insulators on the same footing while maintaining spatial resolution.

The article is organized as follows: We first introduce the Hubbard model used as a theoretical description for the different material types as well as the hierarchy of correlations, the proof of concept involving superlattices constructed by different semiconductors is calculated afterward, and lastly the extension to semiconductor–Mott insulator heterostructures is made.

II. FERMI-HUBBARD MODEL

In order to describe both the strongly correlated Mott insulating and the semiconductor sites we employ a tight-binding

Published by the American Physical Society under the terms of the Creative Commons Attribution 4.0 International license. Further distribution of this work must maintain attribution to the author(s) and the published article's title, journal citation, and DOI.

model, namely the Fermi-Hubbard model [18,44,45],

$$\hat{H} = -\frac{1}{Z}\sum_{\mu\nu s} T_{\mu\nu}\hat{c}^{\dagger}_{\mu s}\hat{c}_{\nu s} + \sum_{\mu} U_{\mu}\hat{n}^{\uparrow}_{\mu}\hat{n}^{\downarrow}_{\mu} + \sum_{\mu s} V_{\mu}\hat{n}_{\mu s}. \quad (1)$$

This Hamiltonian describes the relevant band of the semiconductor, either valence or conduction band, with $U_\mu \equiv 0$, and the Mott insulator with nonzero on-site repulsion $U_\mu \neq 0$. Even if there is a small interaction in the semiconductor this is absorbed into an effective on-site potential V_μ similar to Fermi liquid theory [46,47]. As usual, $\hat{c}^{\dagger}_{\mu s}$ and $\hat{c}_{\nu s}$ denote the fermionic creation and annihilation operators at the lattice sites μ and ν with spin $s \in \{\uparrow, \downarrow\}$ and $\hat{n}_{\mu s}$ are the associated number operators. The hopping matrix $T_{\mu\nu}$ encodes both the adjacency and the hopping strength. In the following, it is assumed in the form of nearest neighbor hopping and zero otherwise. Moreover, we assume a uniform hopping strength throughout the entire heterostructure, but the results can be generalized to nonuniform hopping in a straightforward manner. The coordination number Z counts the nearest neighbors ν for any site μ and is assumed large, $Z \gg 1$. The different regions are differentiated by the two parameters U_μ and V_μ. The Mott insulator is characterized by a large on-site repulsion $U \gg T$, creating the upper and lower Hubbard band, and zero on-site potential $V_\mu \equiv 0$. The semiconductor has an on-site potential $V_\mu \neq 0$, because only the relative positions of the semiconducting and Hubbard bands matter, and no on-site repulsion.

A. Hierarchy of correlations

In the following we are interested in the propagation of electrons through heterostructures. Within the Mott insulating layers this propagation happens by quasiparticles, namely doublons $|\uparrow\downarrow\rangle$ in the upper Hubbard band and holons $|0\rangle$ in the lower Hubbard band on top of a half-filled background [23]. This is similar to the Hubbard-I approximation [18,48]. To this end, we consider the reduced density matrices for one $\hat{\rho}_\mu$, two $\hat{\rho}_{\mu\nu}$, and more lattice sites. This is done by tracing out all other lattice sites but one, $\hat{\rho}_\mu = \mathrm{tr}_{\not\mu}\hat{\rho}$. Additionally, we split up the correlations, $\hat{\rho}_{\mu\nu} = \hat{\rho}_\mu\hat{\rho}_\nu + \hat{\rho}^{\mathrm{corr}}_{\mu\nu}$, and so on. From this starting point, we employ an expansion into powers of the inverse coordination number $1/Z$ based on the $Z \gg 1$ assumption. Doing so, higher-order correlations are successively suppressed. While the two-site correlations scale as $\hat{\rho}^{\mathrm{corr}}_{\mu\nu} = O(1/Z)$, the three-site ones scale as $\hat{\rho}^{\mathrm{corr}}_{\mu\nu\lambda} = O(1/Z^2)$, and so on. This hierarchy yields an iterative scheme for the correlations. Mathematically speaking, we start from the exact evolution equations for these correlations ($\hbar = 1$),

$$\begin{aligned} i\partial_t\hat{\rho}_\mu &= F_1\big(\hat{\rho}_\mu, \hat{\rho}^{\mathrm{corr}}_{\mu\nu}\big), \\ i\partial_t\hat{\rho}^{\mathrm{corr}}_{\mu\nu} &= F_2\big(\hat{\rho}_\mu, \hat{\rho}^{\mathrm{corr}}_{\mu\nu}, \hat{\rho}^{\mathrm{corr}}_{\mu\nu\lambda}\big), \end{aligned} \quad (2)$$

that we get from the Heisenberg equation. We now approximate them using the expansion into the inverse powers of the coordination number. The functions F_n are determined by the Hamiltonian of the system Eq. (1), or more precisely by the commutator with the reduced density matrix. Starting the iterative scheme to lowest order $O(Z^0)$, the evolution equation for the on-site density matrix is given by $i\partial_t\hat{\rho}_\mu = F_1(\hat{\rho}_\mu, 0) + O(1/Z)$. Its zeroth-order solution $\hat{\rho}^0_\mu$ yields the mean-field background as the starting point for the higher orders. For the sake of the Mott insulator description at half-filling and in the regime of large repulsion $U \gg T$, the mean-field ansatz we choose is

$$\hat{\rho}^0_\mu = \frac{|\uparrow\rangle_\mu\langle\uparrow| + |\downarrow\rangle_\mu\langle\downarrow|}{2}. \quad (3)$$

There is one particle per site without any spin ordering. The semiconductor is represented by $\hat{\rho}^0_\mu = |\uparrow\downarrow\rangle_\mu\langle\uparrow\downarrow|$ for the valence band and by $\hat{\rho}^0_\mu = |0\rangle_\mu\langle 0|$ for the conduction band (at zero temperature). Note that the two cases are related to each other via particle-hole duality. For more details see [23,41].

B. Quasiparticle operators

To first order $O(Z^{-1})$, the correlation functions obey $i\partial_t\hat{\rho}^{\mathrm{corr}}_{\mu\nu} = F_2(\hat{\rho}^0_\mu, \hat{\rho}^{\mathrm{corr}}_{\mu\nu}) + O(1/Z^2)$ on top of the mean-field background. For a more detailed view see, e.g., [41–43].

To analyze the evolution of the quasiparticles it is beneficial to introduce the quasiparticle and hole operators

$$\hat{c}_{\mu sI} = \hat{c}_{\mu s}\hat{n}^I_{\mu\bar{s}} = \begin{cases} \hat{c}_{\mu s}(1-\hat{n}_{\mu\bar{s}}), & \text{for} \quad I = 0, \\ \hat{c}_{\mu s}\hat{n}_{\mu\bar{s}}, & \text{for} \quad I = 1, \end{cases} \quad (4)$$

where $\bar{s}$ denotes the spin state opposite to s. They create doublons ($I = 1$) or holons ($I = 0$). Note that these operators are approximately but not exactly equal to the quasiparticle creation and annihilation operators for holons and doublons; see, e.g., [17]. The idea of such effective operators that better describe the physical excitations goes back to Hubbard X operators [48,49] and composite operators [50].

In terms of these operators, we are able to write down the evolution equation for the correlation functions $\langle\hat{c}^{\dagger}_{\mu sI}\hat{c}_{\nu sJ}\rangle^{\mathrm{corr}}$. They consist of a homogeneous part coupling the different correlations and stationary source terms that are not needed to describe the propagation of the quasiparticles. The source terms can be used to calculate ground state correlations. Moreover, it can be shown that the factorization

$$\langle\hat{c}^{\dagger}_{\mu sI}\hat{c}_{\nu sJ}\rangle^{\mathrm{corr}} = p^*_{\mu sI}p_{\nu sJ}, \quad (5)$$

where the factors $p_{\nu sI}$ obey the simple equation

$$\big(i\partial_t - U^I_\mu - V_\mu\big)p_{\mu sI} = \frac{-1}{Z}\sum_{\nu J} T_{\mu\nu}\big\langle\hat{n}^I_{\mu\bar{s}}\big\rangle^0 p_{\nu sJ}, \quad (6)$$

yields the same dynamics; for details see [23]. Furthermore, we assume a highly symmetric lattice such as a hypercubic one, to apply a Fourier transformation of the dependency parallel to the interfaces in the system. It reads

$$\begin{aligned} p_{\mu sI} &= \frac{1}{\sqrt{N^\parallel}}\sum_{\mathbf{k}^\parallel} p^I_{n,\mathbf{k}^\parallel,s}e^{i\mathbf{k}^\parallel\cdot\mathbf{x}^\parallel_\mu}, \\ T_{\mu\nu} &= \frac{Z}{N^\parallel}\sum_{\mathbf{k}^\parallel} T_{m,n,\mathbf{k}^\parallel}e^{i\mathbf{k}^\parallel\cdot(\mathbf{x}^\parallel_\mu - \mathbf{x}^\parallel_\nu)}, \end{aligned} \quad (7)$$

and for isotopic nearest neighbor hopping $T^\parallel_n = T^\perp_{n,n-1} = T$ the components read

$$\begin{aligned} T_{m,n,\mathbf{k}^\parallel} &= \frac{T^\parallel_{\mathbf{k}^\parallel}}{Z}\delta_{m,n} + \frac{T}{Z}(\delta_{n,n-1} + \delta_{n,n+1}), \\ T^\parallel_{\mathbf{k}^\parallel} &= 2T\sum_{x_i}\cos(p^\parallel_{x_i}) \equiv ZT^\parallel_{\mathbf{k}}, \end{aligned} \quad (8)$$

with the hopping contribution $T_{\mathbf{k}}^{\parallel}$. In this hypercubic lattice, there are $Z = 4$ nearest neighbors in a two-dimensional lattice and $Z = 6$ in a three-dimensional one. From Eq. (6) we read of that the different spin sectors decouple; therefore we drop the s and $\mathbf{k}^{\parallel}$ indices for readability and find

$$\begin{aligned}\left(E - U_n^I - V_n\right)p_n^I + \langle \hat{n}_n^I \rangle^0 \sum_J T_{\mathbf{k}}^{\parallel} p_n^J \\ = -T\frac{\langle \hat{n}_n^I \rangle^0}{Z}\sum_J \left(p_{n-1}^J + p_{n+1}^J\right),\end{aligned} \tag{9}$$

where $n \in \mathbb{Z}$ now just labels the lattice sites perpendicular to the interface. These equations show a linear dependency of quasiparticle p_n^1 and hole p_n^0 solutions in the Mott insulator while in the semiconductor one of them is identically zero, in the valence or conduction band, respectively. The assumption of a hypercubic lattice is not only mathematically simplifying the analysis, but also guided by particularly perovskite-like Mott insulators. These show Mott insulating behavior on three-dimensional cubic lattices with $Z = 6$ nearest neighbors, e.g., TiF_3 [26] and $LaTiO_3$ [27].However, we stress that the hierarchy of correlations works for any lattice structure, such that Mott insulators on (quasi-)two-dimensional triangular lattices with $Z = 6$ neighbors [51–53] could also be described.

In those regions of constant U_n or V_n we solve Eq. (9) by

$$p_n^I = \alpha^I e^{i\kappa n} + \beta^I e^{-i\kappa n}. \tag{10}$$

This yields an effective wave number κ perpendicular to the interface. The propagation within the semiconductor with a vanishing repulsion $U_n = 0$ and a constant on-site potential $V_n = V$ is governed by the effective wave number

$$\cos\kappa_{\text{semi}} = \frac{Z}{2T}[V - E - T_{\mathbf{k}}^{\parallel}]. \tag{11}$$

This is a bandlike dispersion relation with $E = V - T_{\mathbf{k}}$. The Mott insulator, however, corresponds to a large constant on-site repulsion $U_n = U \gg T$ with a vanishing potential $V_n = 0$. In this case, the effective wave number reads

$$\cos\kappa_{\text{Mott}} = \frac{Z}{2T}\left[\frac{E(U-E)}{E - U/2} - T_{\mathbf{k}}^{\parallel}\right]. \tag{12}$$

The corresponding dispersion in the Mott insulator reads $E = \frac{1}{2}(U - T_{\mathbf{k}} \pm \sqrt{U^2 + T_{\mathbf{k}}^2})$ with the kinetic energy contribution $T_{\mathbf{k}} = T_{\mathbf{k}}^{\parallel} + \frac{2T}{Z}\cos\kappa_{\text{Mott}}$. This dispersion relation falls in line with the ones obtained by other methods like Hubbard-I [48], Roth's two-pole approximation [54], or composite operator methods [55]. In DMFT the $Z \to \infty$ assumption fixes the effective bandwidth of $T/\sqrt{Z}$ [56,57]. Within the hierarchy of correlations, signatures of this effective bandwidth can be seen even in finite dimension. For a fixed effective bandwidth, the asymptotic magnitude of double occupations becomes independent of the dimension after a quantum quench [58]. This suggest the stability of the hierarchy of correlations. Moreover, the role of dimensionality for higher-order corrections (and hence scaling with the power of Z) is investigated in Ref. [58] for cubic lattices. Furthermore, it would be possible to incorporate second-order effects via renormalization of the hopping parameter [41] if necessary, thus ensuring that

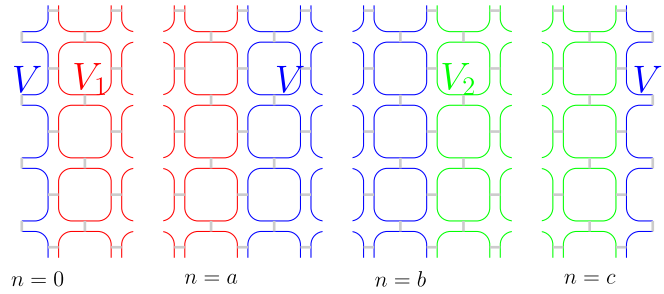

FIG. 1. Two-dimensional schematic of the system signifying the whole system in 2D, or a slice from a three-dimensional lattice; different semiconductors with potential V, V_1, and V_2 are combined to a heterostructure.

out predictions remain valid across these systems. For more details about this and a comparison between the hierarchy of correlations and DMFT see [23]. In the strongly interacting regime $U \gg T$ considered here, real solutions for κ exist only for small $E \approx 0$ (lower Hubbard band) or for $E \approx U$ (upper Hubbard band).

The dispersion relations found above for the doublons and holons are the starting point to calculate their transmission through different types of heterostructures, made up either by different semiconductors or semiconductors and Mott insulators.

III. SEMICONDUCTOR HETEROSTRUCTURE

As proof of principle, we reproduce some well-known results [5] using the hierarchy of correlations. We consider a pure semiconductor structure matching previous studies employing the transfer matrix method [5], which often involve superlattices with numerous wells. The schematic representation of our structure is presented in Fig. 1. There is one type of semiconducting material with on-site potential V functioning as the leads for sites $n \in (-\infty, 0]$ and $n \in [c+1, \infty)$, as well as the connecting layer $n \in [a+1, b]$. It connects two different layers with V_1 in $n \in [1, a]$ and V_2 in $n \in [b+1, c]$. As mentioned, we assume a uniform hopping strength T across the entire lattice, although this restriction could be lifted straightforwardly. In the following analysis, the solution for the semiconductor given by Eq. (9) is denoted as $s_{\pm}^n = e^{\pm i\kappa_{\text{semi}} n}$, with the wave vector defined in Eq. (11). Additionally, $s_{j\pm}$, with $j = 1, 2$, provide the solution in the intermediate regions characterized by potentials V_1 and V_2. Without normalization, the ansatz we use is

$$p_n^0 = \begin{cases} s_+^n + Rs_-^n, & n \leqslant 0, \\ As_{1+}^n + Bs_{1-}^n, & 0 < n \leqslant a, \\ Cs_+^n + Ds_-^n, & a < n \leqslant b, \\ Es_{2+}^n + Fs_{2-}^n, & b < n \leqslant c, \\ \mathcal{T}s_+^n, & c < n, \end{cases} \tag{13}$$

as s_+ describes right-propagating and s_- left-propagating solutions. From Fig. 1 and Eq. (9) we read of boundary equations at the four interfaces and solve for the transmission amplitude $\mathcal{T}$ (see Appendix A 1 for the boundary conditions and the expression for the transmission amplitude).

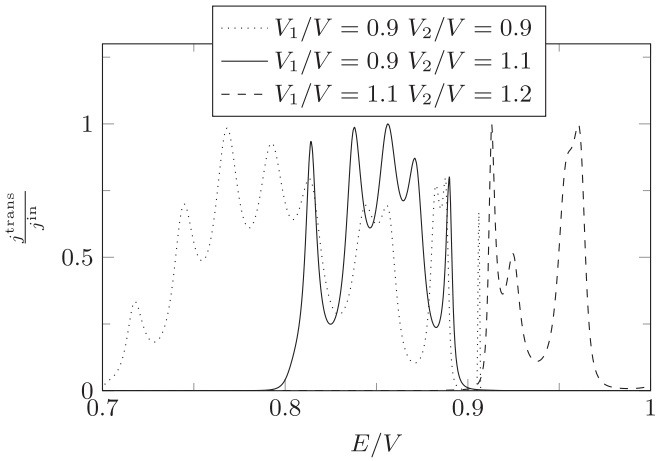

FIG. 2. Transmission as a function of electron energy through the semiconductor heterostructure of various band offsets. We use $Z = 4$ for a two-dimensional problem and $T/V = 0.3$, $a = 7$, $b = 10$, $c = 17$. The bandwidth of the "leads" is given by the plot range.

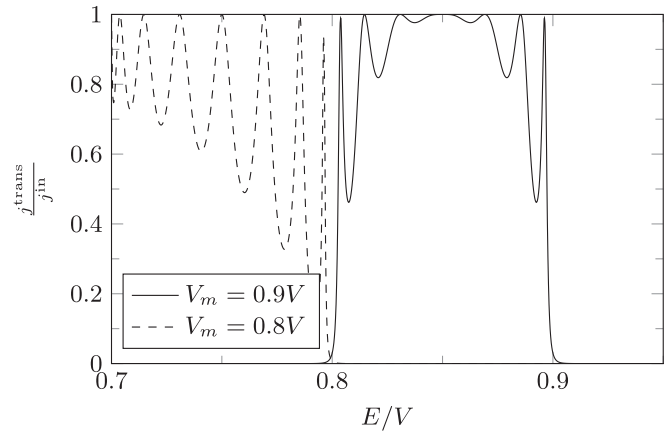

FIG. 3. Transmission as a function of energy through the structure with two types of semiconductors. We use $Z = 4$ for a two-dimensional problem and $T/V = 0.3$ and $a = 7$. The gate potential is $V_m/V = 0.9$ (solid) and $V_m/V = 0.8$ (dashed) and the hopping within the gate is $T_m/V = 0.1$.

The effective wave number Eq. (11) for the semiconducting layers shows that evanescent solutions have $|\kappa_s| \propto \ln V$. The stronger the band mismatch, the stronger the suppression of tunneling. In combination with the injected energy of the plane wave $E \in [V, V - T]$ and a sufficiently large filtering layer V_1 and V_2, all energies $E > \min\{V_1, V_2\}$ get filtered out if $V_1, V_2 < V$. In Fig. 2, this is shown exemplarily for $V_1 = V_2 = 0.9V$ (dotted curve) and a fixed $k^{\parallel}$; for $E < V_1$ there is nearlyzero transmission. There are exponentially small tunnel currents. Otherwise, for $V_1 < V < V_2$ there might be an overlap in the bands around V_1. Consequently, everything outside of this overlap gets filtered out; see solid curve in Fig. 2. Using $V_1, V_2 > V$ on the other hand, everything below $E < \max\{V_1, V_2\} - T$ gets filtered out; see the dashed curve in the same figure. In all three difference scenarios, there are a lot of oscillations in the transmission. Changing the layer thickness by changing a, b, and c does not qualitatively change the results.By including more and more structure to create a superlattice [5] these oscillations can be smoothed out and we would find real transmission minibands, because there is more constructive interference in these superlattices than in the small system here.

If the hopping is not isotropic, it is possible to achieve the same energy filtering with just two types of semiconductors. The filtering regions ought to have smaller hopping than the leads. This then results in symmetric transmission minibands. With isotropic hopping this system is only capable of filtering out energies above a certain value.

Smaller structure: Nonisotropic hopping

As mentioned, in the case of nonisotropic hopping the energy filtering effect and minibands can be achieved by a structure consisting of only two different semiconductors: one acting as the leads and another one with smaller hopping as the gate. With a similar ansatz as for the bigger structure with $s_\pm$ and $m_\pm$ describing the solutions in the leads and the gate, respectively, we find the transmission amplitude

$$\mathcal{T} = \frac{(m^2-1)(s^2-1)m^{a+1}s^{-a-1}}{(ms-1)^2 - m^{2a+2}(m-s)^2}. \tag{14}$$

It is exemplarily shown in Fig. 3 for sample parameters $V_m/V = 0.9$ and $T/T_m = 3$. By shifting the gate potential and thus the band overlap this setup can filter all energies above or below a certain energy or produce transmission minibands. These can only be symmetric.

IV. MOTT–SEMICONDUCTOR STRUCTURE

Having successfully demonstrated our method for a well-studied case of a semiconductor structure, our focus now shifts toward investigating a Mott insulator–semiconductor heterostructure. In this new configuration, semiconducting leads, serving as source and drain terminals, encase a Mott insulating material characterized by an on-site repulsion parameter denoted as U. Within this insulating region, there exists another semiconductor segment controlled by a gate voltage V_m. A schematic representation of this structure is provided in Fig. 4(a). Figure 4(b) shows the band edges of the lead, drain, and gate relative to the Hubbard bands of the Mott insulating layers. Notably, the application of a gate voltage results in a shift of the (red) band within the middle region, denoted as $V_m - T_{\mathbf{k}}$, thereby modifying the transmission characteristics.

Again, we use a plane wave ansatz for the different semiconducting and the Mott insulating regions, the source and drain $s_\pm$, the Mott insulating layers $r_\pm$, and the gate voltage region $m_\pm$. Hence, the ansatz is given by

$$p_n^0 = \begin{cases} s_+^n + Rs_-^n, & n \leqslant 0, \\ Ar_+^n + Br_-^n, & 0 < n \leqslant a, \\ Cm_+^n + Dm_-^n, & a < n \leqslant b, \\ Er_+^n + Fr_-^n, & b < n \leqslant c, \\ \mathcal{T}s_+^n, & c < n. \end{cases} \tag{15}$$

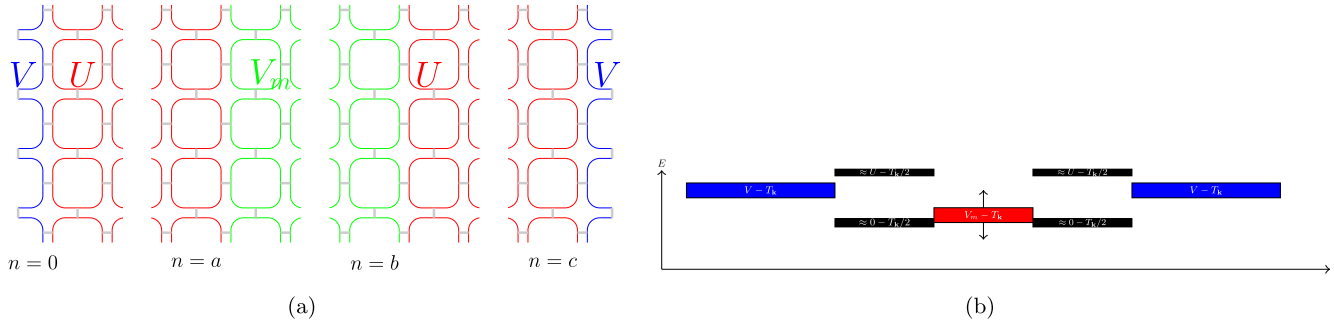

FIG. 4. One semiconductor with a gate voltage V_m between the same Mott insulating material U; everything is connected to a source and drain lead V. (a) Real-space lattice of the structure signifying the whole system in 2D, or a slice from a three-dimensional lattice. (b) Energy spectrum. The gate potential V_m is adjustable by a voltage.

The solutions in the various regions are in accordance to Eqs. (16) and (12) and thus given by

$$s_\pm = e^{i\kappa_{\text{semi}} n},\ \cos\kappa_{\text{semi}} = \frac{Z}{2T}[V - E - T_{\mathbf{k}}^{\parallel}], \tag{16}$$

$$m_\pm = e^{i\kappa_{\text{m}} n},\ \cos\kappa_{\text{m}} = \frac{Z}{2T}[V_m - E - T_{\mathbf{k}}^{\parallel}], \tag{17}$$

$$r_\pm = e^{i\kappa_{\text{Mott}} n},\ \cos\kappa_{\text{Mott}} = \frac{Z}{2T}\left[\frac{E(U-E)}{E - U/2} - T_{\mathbf{k}}^{\parallel}\right]. \tag{18}$$

Due do the different structure the boundary conditions obtained from Eq. (9) change (see Appendix A 2). The transmission amplitude we find reads

$$\mathcal{T}(E, k^{\parallel}) = \frac{(m^2-1)(r^2-1)^2(s^2-1)(-m^{a+b})r^{a+b+c+1}}{s^{c+1}(W_1 + W_2)} \tag{19}$$

with long expressions W_1 and W_2 given in Appendix A 2. The transmitted current is given by the absolute square $|\mathcal{T}(E, k^{\parallel})|^2$ [23], because the leads have the same effective wave number.

A. Transmittance

In the current context, we can discern three primary scenarios. First, the potential at the source and drain terminals, denoted as V, may fall below the lower Hubbard band. Alternatively, it could lie within the region between the two bands. Lastly, it might exceed the upper Hubbard band. Additionally, there is a possibility that the potential is (partially) situated within one of the two Mott bands. In this case, the presence of such a potential configuration results in the emergence of a transmission channel. The discussion can be simplified substantially by using the particle-hole symmetry [23] in the Mott insulating layers. The particle p_n^1 and hole p_n^0 solutions are related via $(E-U)p_n^1 = Ep_n^0$ which shows the symmetry around $U/2$, the middle of the band gap. Therefore, it is enough to look at three different cases: V below lower Hubbard band, V inside lower Hubbard band, and V inside the Mott gap but below $U/2$. The other ones can be obtained by the symmetry operation of inversion at the $U/2$ energy with appropriately shifting the on-site potentials.In the following, we will use $T = 0.3U$ as the hopping strength, measured in units of the Coulomb interaction, which is providing the energy scale. This yields an effective strength of $T/Z = 0.075U$. This is in the same range as in other studies using $0.05 < T/U < 0.2$ [39,40,59–61]. Moreover, the qualitative behavior turns out to be independent of the hopping strength, as long as the parameter choice stays within the strongly correlated Mott insulator regime. Therefore, we believe that the discussion below is transferable to other parameter combinations.

1. $V = -0.3U$: Below lower Hubbard band

Using $V = -0.3U$ and a specific parallel momentum value $k^{\parallel}$, the transmittance exhibits a pronounced peak. This resonance energy shifts with the gate potential V_m. It is important to note that these resonant states do not manifest for all values of V_m. Instead, we observe them solely within a range of gate potentials $-0.4 < V_m/U < -0.2$ [Fig. 5(a)]. The resonances only appear if there is a band overlap between the leads and the gate, as they stem from constructive interference within the gate region.

2. $V = 0U$: Lower Hubbard band

In the $V = 0U$ case, the lead bands cover the lower Hubbard band fully covered, but reach down further in energy. By varying the gate potential V_m we find peaks below the lower Hubbard band; see Fig. 5(b). Inside the lower Hubbard band there is a transmission channel with nearly constant transmission for all gate potentials; they only differ in the absolute value of the transmission. Above the band, transmission sharply drops off to zero (besides exponentially small tunneling currents).

3. $V = 0.3U$ and $V = 0.7U$: Inside Mott gap

In [23], it was demonstrated that there is exactly zero transmission through Mott layers in the middle of the Mott gap $E = U/2$ with an unpolarized spin background, which is the case here. At this particular energy level, a perfect destructive interference between particle and hole currents occurs. Consequently, it is crucial to differentiate between situations where the energy is below or above this specific point. In Fig. 5(c), we observe the first scenario, where the energy is below the midpoint of the band gap. Similar to previous observations, a peaked transmission structure is obtained for specific values of the gate potential V_m, while for other values, the transmission remains nearly constant close to zero.

For the second scenario, where the energy is above the midpoint of the band gap, refer to Fig. 5(d). The symmetry

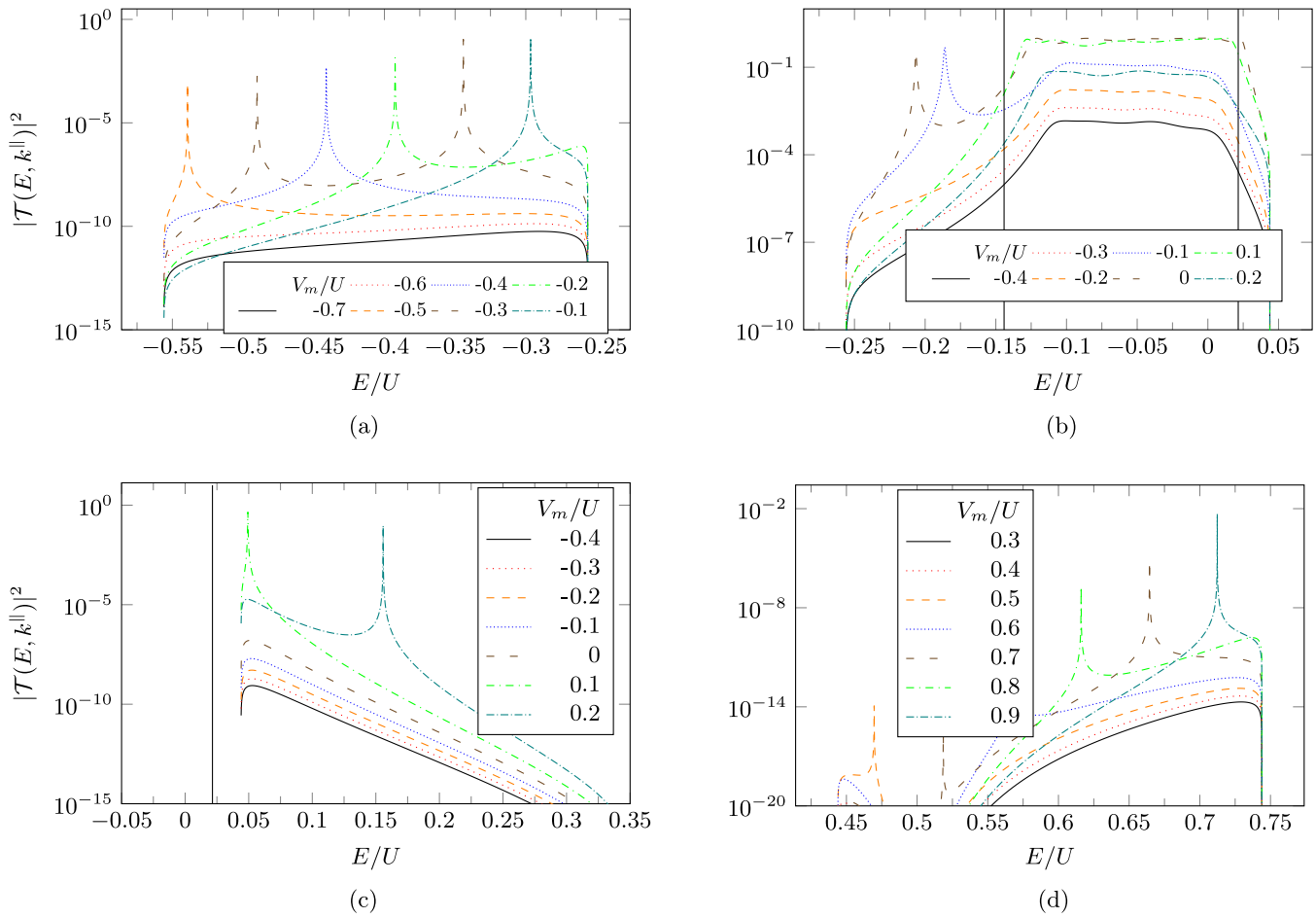

FIG. 5. Transmission for $k^{\parallel} = \pi/4$ through the semiconductor–Mott heterostructure as a function of electron energy for different on-site potentials relative to the Hubbard bands. The plot range always gives the band of the source/drain; the different colors depict different V_m/U. Vertical lines depict the Hubbard bands, if lying in the depicted range. The parameters are $T = 0.3U$, $Z = 4$, $a = 2$, $b = 5$, $c = 6$. (a) With $V = -0.3U$ the energy range is below the lower Hubbard band. (b) With $V = 0U$ the lower Hubbard band is fully covered. (c) The electron energy is in between the two Hubbard bands, below the point $E = U/2$. (d) The electron energy is in between the two Hubbard bands, above the point $E = U/2$.

between to two cases below and above the midpoint of the Mott gap can be seen.

B. Resonances

In the various scenarios discussed above, we observe peaks or resonances in the transmittance outside the Mott bands. Because of this, these resonances can only arise from constructive interference within the gate and should fulfill $\kappa_m d = n\pi$. Here, κ_m is the wave number, d is the thickness of the gate layer, and $n \in \mathbb{Z}$ is an integer. These conditions lead to resonance energies E_{res} given by

$$E_{\text{res}} = \frac{-2T\cos(k^{\parallel}) + V_m Z - 2T\cos\left(\frac{\pi n}{d}\right)}{Z}. \tag{20}$$

However, when comparing these predicted resonance energies to the actual ones, $E_{\text{res}}^{\text{real}}$ obtained from $|\mathcal{T}|^2$ [Fig. 6(a)], we notice discrepancies. Assuming the correctness of the resonance energy formula, we introduce a renormalized gate voltage $V_m^r = V_m + a(V_m)$. Here, if $a(V_m)$ is negative, it signifies a downward shift in the gate voltage. In Fig. 6(b), we present $a(V_m)$ for different cases where $|V_m - V| \leqslant T$, ensuring an overlap between the source/drain and gate bands to maintain resonances. Several observations can be made:

(a) If the energy falls inside one of the Mott bands, it opens up a transmission channel throughout the structure. Thus the effective width of the region wherein constructive interference happens is larger than the gate region. This renders the resonance energy formula Eq. (20) wrong, because there might be modes fitting in more than one region now. The renormalization $a(V_m)$ compensates for this effect.

(b) Outside the Mott bands, where the thickness of the layer is solely given by the gate region, the renormalization pushes the effective gate potential V_m away from the bands. Below the lower band, it is pushed toward smaller values with $a(V_m) < 0$, while above the upper band, it is pushed toward larger values with $a(V_m) > 0$.

(c) Between the two Mott bands, a change in sign occurs at $\approx U/2$ (the shift is due to $k^{\parallel} \neq 0$). Below this point, $a(V_m)$ is positive, while above it, $a(V_m)$ is negative. Inside the Mott gap the effective gate potential is pushed toward the middle of the gap.

Overall, these trends are consistent across different $V_m - V$ cases, with small deviations attributable to numerical con-

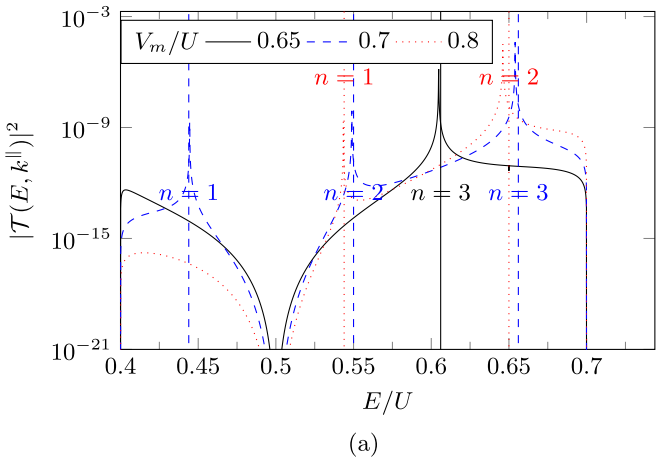

(a)

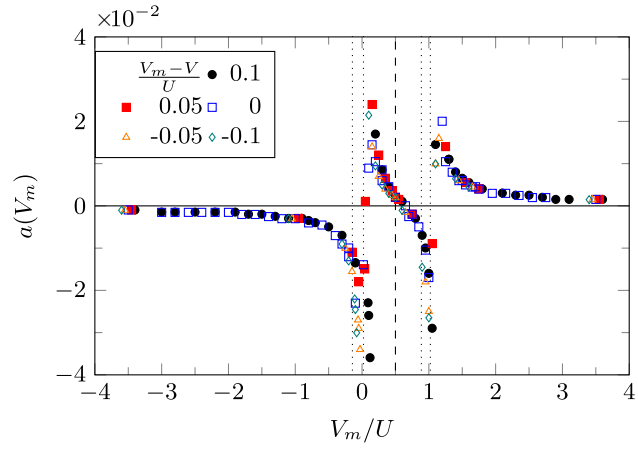

(b)

FIG. 6. (a) Transmittance vs predicted resonance energies. The panel gives the transmittance as function of energy for a lead potential $V = 0.7U$ together with the resonance energies predicted by Eq. (20) as dashed vertical lines for different gate potentials V_m. Panel (b) gives the renormalization parameter $a(V_m)$ of the gate voltage for various combinations of V and V_m. The dashed line marks $U/2$; the dotted lines give the Mott bands. The parameters are $T = 0.3U$, $Z = 4$, $a = 2$, $b = 5$, $c = 6$, $k^{\parallel} = \pi/4$.

siderations. Thus, there is no dependency on the specific distance $V_m - V$, and only the relative position of the gate voltage V_m with respect to the Mott bands is of significance. Far away from the bands the renormalization goes to zero $a(V_m \gg U) = a(V_m \ll 0) \to 0$.

C. Scattering phase

In order to obtain the renormalized gate potential to explain the shift between the predicted and real resonances we need to assume the correctness assumed $\kappa_m d = n\pi$ to be valid. This is different for the phase accumulation model for quantum wells [62–64]: There, the scattering phase $\delta(E)$ modifies the resonance condition to

$$\kappa_m d = n\pi + \delta(E). \tag{21}$$

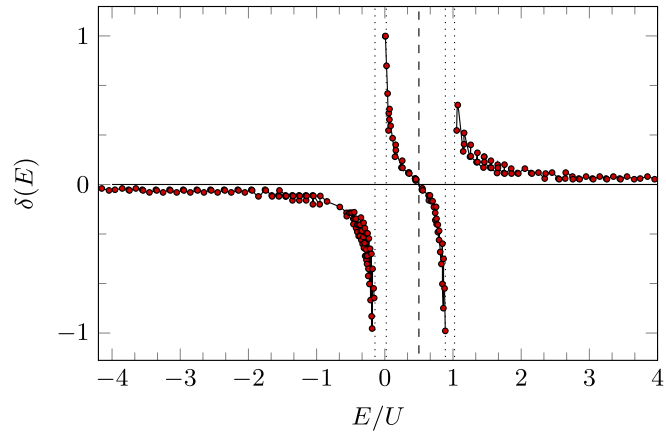

FIG. 7. Phase shift $\delta(E)$ for $V = V_m$. The dashed line marks $U/2$; the dotted lines give the Mott bands.

This scattering phase is energy dependent and leads to resonance energies described by

$$E^{\delta}_{\text{res}} = \frac{-2T\cos(k^{\parallel}) + V_m Z - 2T\cos\left(\frac{\pi n+\delta(E)}{d}\right)}{Z}. \tag{22}$$

From these resonance energies, we can deduce the behavior of the scattering phase, $\delta(E)$, as depicted in Fig. 7. The energy range is covered by tuning the lead potential V. Notably, like the renormalization of the potential, the scattering phase undergoes a sign change at the Mott bands and at $U/2$. As one moves far away from the Mott bands, the scattering phase tends to zero. Functionally, the energy-dependent scattering phase $\delta(E)$ depends on the bandwidth contribution $W = \frac{2T}{Z}$ from the hopping orthogonal to the interfaces. With this, it reads

$$\delta(E) = \begin{cases} \frac{W}{2}\frac{1}{E+\frac{W}{2}}, & E < \text{lower Hubbard band}, \\ -W\tan\left(\pi\left[\frac{E}{U} - \frac{U}{2}\right]\right), & \text{between Hubbard bands}, \\ \frac{W}{2}\frac{1}{E-U+\frac{W}{2}}, & E > \text{upper Hubbard band}. \end{cases} \tag{23}$$

As expected, the maximum of the derivative of the scattering phase coincides with the Mott bands. This observation is in line with the fact that this quantity essentially describes the density of states [65].

From the scattering phase and the wave vector κ, we can also compute the scattering length $a_s(\kappa) = \frac{-\tan[\delta(\kappa)]}{\kappa}$. Figure 8 shows the scattering phase $\delta(\kappa)$ together with $a_s(\kappa)$. There are several branches of the momentum-dependent scattering phase $\delta(k)$ (blue squares) that show a linear dependence on the wave number. For every branch the scattering length thus is given by $a_s(\kappa) \propto \tan(\text{const}_1\kappa + \text{const}_2)/\kappa$ (red circles).

D. Parallel momentum integrated transmission

In practical real-world setups, controlling the value of $k^{\parallel}$ for electrons can be challenging. The electrons occupy all possible parallel momentum values, and in order to incorporate the fact that $k^{\parallel}$ is not resolved, we will consider transmission

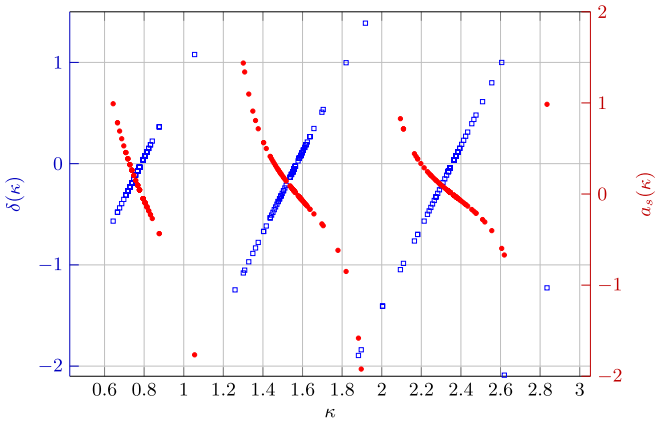

FIG. 8. Phase shift $\delta(\kappa)$ (blue squares, left axis) and scattering length $a_s(\kappa)$ (red circles, right axis) for $V = V_m$. The oscillations are an artifact of the energy resolution used in the analysis.

probabilities that are averaged over $k^{\parallel}$, denoted as $\mathcal{T}(E)$:

$$\mathcal{T}(E) = \frac{1}{N} \int \mathcal{T}(E, k^{\parallel})\, dk^{\parallel}. \tag{24}$$

The resulting transmittance represents a superposition of individual transmission probabilities, leading to a superposition of peaks in the transmission spectrum. Tuning the gate voltage V_m shifts the region of appreciable transmission to either lower or higher energies.

For example, when $V_m = 0.9U$ [Fig. 9(a)], we observe a shift toward higher energies in the transmission spectrum for $V = 0.7U$. Conversely, when V_m is adjusted to $0.5U$, the transmission spectrum shifts toward lower energies. Also, the magnitude of the transmission goes down. Away from the occurring maximum transmittance, there is an exponential drop-off.

Additionally, the higher peak in the transmission spectrum can also be shifted by varying the gate voltage, as demonstrated in Fig. 9(c). In this case, transitioning from $V_m = 0.2U$ to $0.4U$ causes the highest transmission peak to shift followed by an exponential tail, here to higher energies. This exponential decay acts as the envelope of transmission peaks.

However, it is crucial to note that these observations primarily apply outside the Mott bands. Inside the Mott bands, changing the gate voltage tends to result in relatively flat transmission curves, as depicted in Fig. 9(b). The alteration in gate voltage primarily affects the overall magnitude of transmission and the offset from zero outside the Mott bands. Changing the layer thickness by changing a, b, and c does not qualitatively change the results. Transmission channels stay open, only evanescent waves yield a lower transmission with increasing the layer thickness.

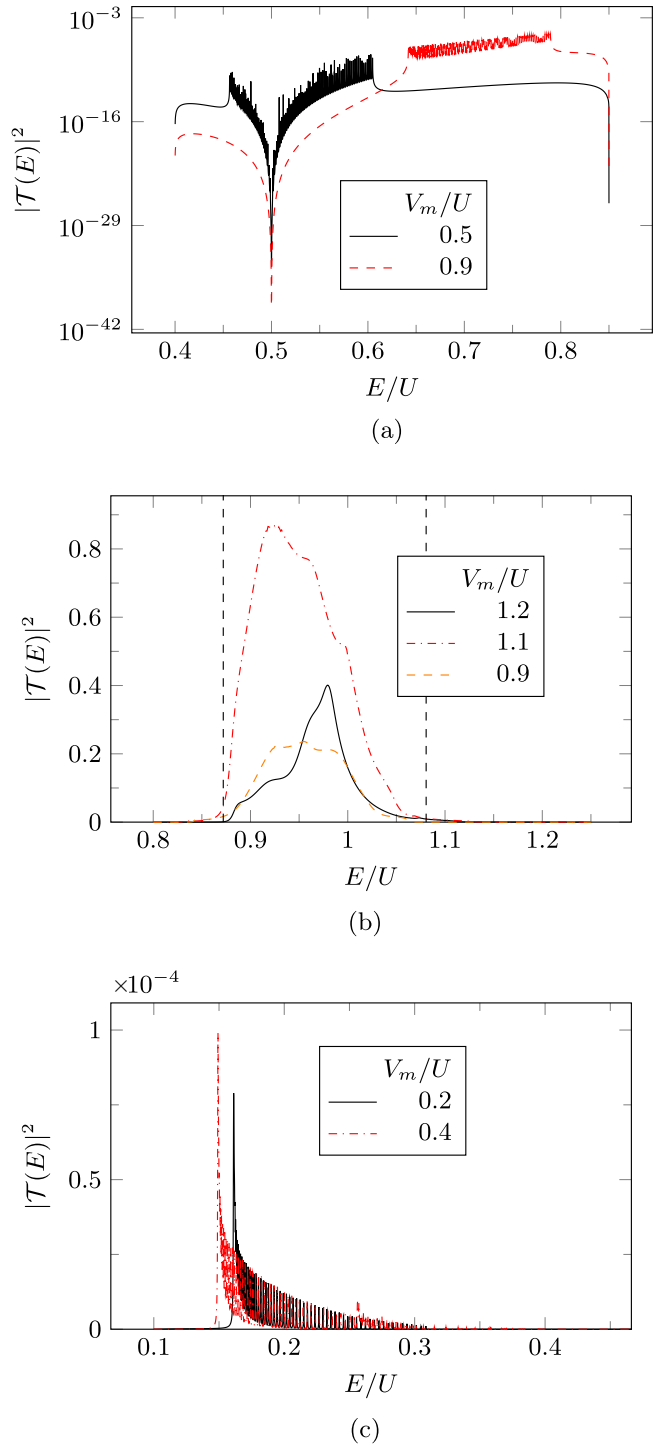

FIG. 9. Parallel momentum averaged transmittance for different source/drain potentials V as a function of electron energy. Dashed lines mark the edges of the upper Hubbard band. The parameters are $T = 0.3U$, $Z = 4$, $a = 2$, $b = 5$, $c = 6$. (a) $V = 0.7U$. (b) $V = 1.1U$. (c) $V = 0.4U$.

E. Applying an overall voltage

Finally, we introduce a global voltage to the entire system. As depicted in Fig. 10 there is a potential difference between the source V_S and the drain V_D creating the driving voltage. This alters the on-site potential in all the layers, also affecting the Mott layers. Figure 10 shows a small applied voltage shifting the right Mott layer relative to the left one. Inside the layers, for simplicity, the potential is assumed constant. For small fractions of voltage over system size this seems reasonable. With more sophisticated methods to solve all the boundary equations (e.g., transfer matrices) this can easily be

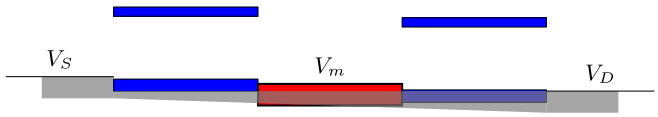

FIG. 10. "Band structure" of the system with applied voltage; the drain V_D is lower than the source V_S; the gate potential V_m is still adjustable. The applied voltage also shifts the Mott bands. Here, a linear behavior is assumed while inside the distinctive regions the potential is taken to be constant.

refined.Consequently, we find the transmittance $T(E)$ as

$$T(E) = |\mathcal{T}(E)|^2 \frac{\sin(\kappa_D)}{\sin(\kappa_S)}. \tag{25}$$

The additional factor $\frac{\sin(\kappa_D)}{\sin(\kappa_S)}$ comes because the effective wave numbers and thus the group velocities are not the same within the source and the drain.

Figure 11 shows the transmission for some exemplary values of the source, drain, and gate potential. The gate voltage can be used to tune the energy range of the transmission. This is true within the energy range of the Mott bands and outside.

Even though our analysis was done at zero temperature, the thermal energy of the quasiparticles $k_B T_{\mathrm{qp}}$ is much smaller than the Mott gap, $k_B T_{\mathrm{qp}} \ll U$ for typical materials. The quasiparticle structure remains valid even in the presence of scattering [43], and therefore equilibration may be described inside the Mott bands, as well as at the source and drain, by applying a Fermi distribution $f(T_{\mathrm{qp}})$. In the end, finite-temperature results may be obtained by a convolution of the transmission $T(E)$ with $f(T_{\mathrm{qp}})$.

V. CONCLUSIONS

In summary, we studied different types of heterostructures built by Mott insulators with on-site Coulomb repulsion U and semiconductors with on-site potential V. The hierarchy-of-correlations approach allows us to treat the strongly interacting Mott insulators and the weakly interacting semiconductors within the same framework. Using this formal expansion into the inverse coordination number $1/Z$, we can assign effective wave vectors to the quasiparticles allowing us to calculate the transmission probability through various types of structures with and without an applied voltage.

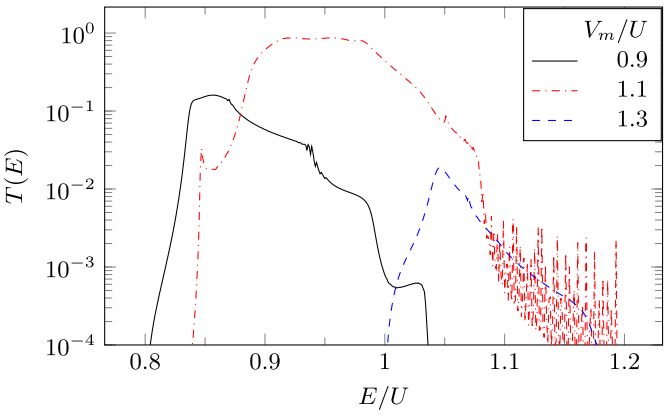

FIG. 11. Transmission through the semiconductor–Mott heterostructure with an applied voltage for a source potential $V_S = 1.1U$ and a drain potential $V_D = 0.7U$ as a function of energy for different gate potentials. The parameters are $T = 0.3U$, $Z = 4$, $a = 2$, $b = 5$, $c = 6$.

For a semiconductor structure, our approach reproduces the well-known result of transmission through minibands.

The Mott insulator–semiconductor heterostructure, on the other hand, allows us to make use of the strong suppression of the quasiparticle current due to destructive interference of the particle and hole channels in the middle of the Mott insulator band gap. Within a phase accumulation model for quantum wells we determine analytical expressions for the resonance energies which depend on the energy relative to the Mott bands.

Looking at the transmission curves integrated over parallel momentum, we find a skewness in the transmission function around its center that could have possible applications in thermoelectric devices. The energies for which transmission is found can be tuned by the gate. In this setting, the skewness of the transport distribution function is desirable as it helps to increase the Seebeck coefficient [16]. This feature distinguishes heterostructures with a Mott insulator, i.e., with strongly interacting electrons, from a pure semiconductor structure.

ACKNOWLEDGMENTS

The authors thank F. Queisser and R. Schützhold for fruitful discussions and valuable feedback on the manuscript. Funded by the Deutsche Forschungsgemeinschaft (DFG, German Research Foundation), Project ID 278162697, SFB 1242.

DATA AVAILABILITY

The data that support the findings of this article are not publicly available. The data are available from the authors upon reasonable request.

APPENDIX

1. Semiconductor structure

From Eq. (9) we can deduct two boundary equations per interface for the structure shown in Fig. 1—one for the lattice site left of the interface and one to the right of it. In this case the eight equations read (after some algebra)

$$s_{1+}B + \frac{A}{s_{1+}} = \left(\frac{1}{s_+} + Rs_+\right), \tag{A1}$$

$$1 + R = (A + B), \tag{A2}$$

$$As_{1+}^{a+1} + \frac{B}{s_{1+}^{a+1}} = \left(Cs_+^{a+1} + \frac{D}{s_+^{a+1}}\right), \tag{A3}$$

$$Cs_+^a + \frac{D}{s_+^a} = \left(As_{1+}^a + \frac{B}{s_{1+}^a}\right), \tag{A4}$$

$$Cs_+^{b+1} + \frac{D}{s_+^{b+1}} = \left(sr_{2+}^{b+1} + \frac{F}{s_{2+}^{b+1}}\right), \tag{A5}$$

$$Es_{2+}^b + \frac{F}{s_{2+}^b} = \left(Cs_+^b + \frac{D}{s_+^b}\right), \tag{A6}$$

$$E s_{2+}^{c+1} + \frac{F}{s_{2+}^{c+1}} = \mathcal{T} s_{+}^{c+1}, \tag{A7}$$

$$\mathcal{T} s_{+}^{c} = \left(E s_{2+}^{c} + \frac{F}{s_{2+}^{c}} \right). \tag{A8}$$

Inserting the ansatz (13) into this we can solve for the transmission coefficient behind the interface as

$$\mathcal{T} = \frac{-s_{1+}^{a+1}\left(s_{1+}^{2}-1\right)\left(s_{2+}^{2}-1\right)\left(s_{+}^{2}-1\right)^{2} s_{+}^{a+b} s_{2+}^{b+c}}{s_{+}^{1+c}(M_1+M_2+M_3+M_4+M_5+M_6)} \tag{A9}$$

with the six terms

$$M_1 = s_{2+}^{2b}\left\{s_{+}^{2a}\left[s_{1+}^{2a+2}(s_{1+}-s_{+})^2-(s_{1+}s_{+}-1)^2\right]-\left(s_{1+}^{a+1}-1\right)\left(s_{1+}^{a+1}+1\right)s_{+}^{2b+1}(s_{1+}-s_{+})(s_{1+}s_{+}-1)\right\}, \tag{A10}$$

$$M_2 = s_{+}s_{2+}^{2b+2}\left\{s_{+}^{2a+1}\left[s_{1+}^{2a+2}(s_{1+}-s_{+})^2-(s_{1+}s_{+}-1)^2\right]-\left(s_{1+}^{a+1}-1\right)\left(s_{1+}^{a+1}+1\right)s_{+}^{2b}(s_{1+}-s_{+})(s_{1+}s_{+}-1)\right\}, \tag{A11}$$

$$M_3 = s_{2+}^{2c+1}\left\{2s_{+}^{2a+1}\left[s_{1+}^{2a+2}(s_{1+}-s_{+})^2-(s_{1+}s_{+}-1)^2\right]-\left(s_{+}^{2}+1\right)\left(s_{1+}^{a+1}-1\right)\left(s_{1+}^{a+1}+1\right)s_{+}^{2b}(s_{1+}-s_{+})(s_{1+}s_{+}-1)\right\}, \tag{A12}$$

$$M_4 = s_{2+}^{2c+2}\left\{\left(s_{1+}^{a+1}-1\right)\left(s_{1+}^{a+1}+1\right)s_{+}^{2b+1}(s_{1+}-s_{+})(s_{1+}s_{+}-1)+s_{+}^{2a}\left[(s_{1+}s_{+}-1)^2-s_{1+}^{2a+2}(s_{1+}-s_{+})^2\right]\right\}, \tag{A13}$$

$$M_5 = s_{+}s_{2+}^{2c}\left\{\left(s_{1+}^{a+1}-1\right)\left(s_{1+}^{a+1}+1\right)s_{+}^{2b}(s_{1+}-s_{+})(s_{1+}s_{+}-1)+s_{+}^{2a+1}\left[(s_{1+}s_{+}-1)^2-s_{1+}^{2a+2}(s_{1+}-s_{+})^2\right]\right\}, \tag{A14}$$

$$M_6 = s_{2+}^{2b+1}\left\{\left(s_{+}^{2}+1\right)\left(s_{1+}^{a+1}-1\right)\left(s_{1+}^{a+1}+1\right)s_{+}^{2b}(s_{1+}-s_{+})(s_{1+}s_{+}-1)+2s_{+}^{2a+1}\left[(s_{1+}s_{+}-1)^2-s_{1+}^{2a+2}(s_{+}-s_{+})^2\right]\right\}. \tag{A15}$$

The transmission probability is given by the absolute square $|\mathcal{T}|^2$, because the two leads have the same effective wave number.

2. Mott–semiconductor structure with single gate

For the heterostructure combining the two Mott insulating regions U with the gate V_m [see Fig. 4(a)] the boundary conditions change. In the case of a half-filled background we find from Eq. (9) the eight equations

$$\begin{aligned}
\tilde{B} r_{+} + \tilde{A} r_{+}^{-1} &= R s_{+} + s_{+}^{-1}, \\
1 + R &= \tilde{A} + \tilde{B}, \\
\tilde{A} r_{+}^{a+1} + \tilde{B} r_{+}^{-(a+1)} &= C m_{+}^{a+1} + D m_{+}^{-(a+1)}, \\
C m_{+}^{a} + D m_{+}^{-a} &= \tilde{A} r_{+}^{a} + \tilde{B} r_{+}^{-a}, \\
\tilde{E} r_{+}^{b} + \tilde{F} r_{+}^{-b} &= C m_{+}^{b} + D m_{+}^{-b}, \\
\tilde{E} r_{+}^{c+1} + \tilde{F} r_{+}^{-(c+1)} &= \mathcal{T} s_{+}^{c+1}, \\
\mathcal{T} s_{+}^{c} &= \tilde{E} r_{+}^{c} + \tilde{F} r_{+}^{-c}, \\
C m_{+}^{b+1} + D m_{+}^{-(b+1)} &= \tilde{E} r_{+}^{b+1} + \tilde{F} r_{+}^{-(b+1)},
\end{aligned} \tag{A16}$$

where we introduced the abbreviations abbreviations $\{\tilde{A}, \tilde{B}, \tilde{E}, \tilde{F}\} = \frac{E-V-U/2}{E-U-V}\{A, B, E, F\}$. Inserting the ansatz (15) yields the transmission amplitude

$$\mathcal{T}(E, k^{\parallel}) = \frac{(m^2-1)(r^2-1)^2(s^2-1)(-m^{a+b})r^{a+b+c+1}}{s^{c+1}(W_1+W_2)}. \tag{A17}$$

In this, the two long expressions read

$$\begin{aligned}
W_1 = &-\{m^{2a}[r^{2a+3}(r-s)+rs-1][r^{2b}(rs-1)+r^{2c+1}(r-s)]\}-rm^{2a+2}\{r[r^{2a}(r-s)+s]-1\}[r^{2b+1}(rs-1)+r^{2c}(r-s)] \\
&+rm^{2b}\{r[r^{2a}(r-s)+s]-1\}[r^{2b+1}(rs-1)+r^{2c}(r-s)]+m^{2b+2}[r^{2a+3}(r-s)+rs-1][r^{2b}(rs-1)+r^{2c+1}(r-s)], \\
W_2 = &\, m^{2a+1}\{r^{2b+1}(rs-1)[(r^2+1)r^{2a+1}(r-s)+2rs-2]+r^{2c}(r-s)[2r^{2a+3}(r-s)+(r^2+1)(rs-1)]\} \\
&+m^{2b+1}(r^{2b+1}(rs-1)\{-[(r^2+1)r^{2a+1}(r-s)]-2rs+2\}-r^{2c}(r-s)[2r^{2a+3}(r-s)+(r^2+1)(rs-1)]).
\end{aligned} \tag{A18}$$

[1] Z. Lu, D. Lockwood, and J.-M. Baribeau, Quantum confinement and light emission in SiO_2/Si superlattices, Nature (London) **378**, 258 (1995).

[2] M. Willatzen, R. V. Melnik, C. Galeriu, and L. L. Y. Voon, Quantum confinement phenomena in nanowire superlattice structures, Math. Comput. Simul. **65**, 385 (2004).

[3] J. Liu, S. Okamoto, M. van Veenendaal, M. Kareev, B. Gray, P. Ryan, J. W. Freeland, and J. Chakhalian, Quantum confinement of Mott electrons in ultrathin $LaNiO_3/LaAlO_3$ superlattices, Phys. Rev. B **83**, 161102 (2011).

[4] T. Gaylord and K. Brennan, Semiconductor superlattice electron wave interference filters, Appl. Phys. Lett. **53**, 2047 (1988).

[5] Q. Yang and A. Li, Energy filters using modulated superlattices, J. Appl. Phys. **87**, 1963 (2000).

[6] H.-H. Tung and C.-P. Lee, A novel energy filter using semiconductor superlattices and its application to tunneling time calculations, IEEE J. Quantum Electron. **32**, 2122 (1996).

[7] J. Smoliner, R. Heer, and G. Strasser, Biased GaAs/AlGaAs superlattices employed as energy filter for ballistic electron emission microscopy, Surf. Interface Anal. **27**, 542 (1999).

[8] A. M. Kan'an, A. Puri, and T. Odagaki, Transmission of an obliquely incident electron wave through $GaAs/Al_xGa_{1-x}As$ structures: Application to an electron wave filter, J. Appl. Phys. **74**, 370 (1993).

[9] H.-H. Tung and C.-P. Lee, An energy band-pass filter using superlattice structures, IEEE J. Quantum Electron. **32**, 507 (1996).

[10] L. Whitlow and T. Hirano, Superlattice applications to thermoelectricity, J. Appl. Phys. **78**, 5460 (1995).

[11] C. Summers and K. Brennan, Variably spaced superlattice energy filter, a new device design concept for high-energy electron injection, Appl. Phys. Lett. **48**, 806 (1986).

[12] P. Harness, R. Pritchard, B. Khamsehpour, W. Truscott, and K. Singer, Double-barrier resonant tunneling structures incorporating superlattice energy filters, J. Appl. Phys. **71**, 3019 (1992).

[13] C. Gayner and Y. Amouyal, Energy filtering of charge carriers: Current trends, challenges, and prospects for thermoelectric materials, Adv. Funct. Mater. **30**, 1901789 (2020).

[14] N. Neophytou and M. Thesberg, Modulation doping and energy filtering as effective ways to improve the thermoelectric power factor, J. Comput. Electron. **15**, 16 (2016).

[15] Y. Mune, H. Ohta, K. Koumoto, T. Mizoguchi, and Y. Ikuhara, Enhanced Seebeck coefficient of quantum-confined electrons in $SrTiO_3/SrTi_{0.8}Nb_{0.2}O_3$ superlattices, Appl. Phys. Lett. **91**, 192105 (2007).

[16] J.-C. Zheng, Asymmetrical transport distribution function: Skewness as a key to enhance thermoelectric performance, Research (2022) 9867639.

[17] I. Avigo, F. Queisser, P. Zhou, M. Ligges, K. Rossnagel, R. Schützhold, and U. Bovensiepen, Doublon bottleneck in the ultrafast relaxation dynamics of hot electrons in $1T$-TaS_2, Phys. Rev. Res. **2**, 022046(R) (2020).

[18] J. Hubbard, Electron correlations in narrow energy bands, Proc. R. Soc. London A **276**, 238 (1963).

[19] B. Brandow, Electronic structure of Mott insulators, Adv. Phys. **26**, 651 (1977).

[20] V. I. Anisimov, J. Zaanen, and O. K. Andersen, Band theory and Mott insulators: Hubbard U instead of Stoner I, Phys. Rev. B **44**, 943 (1991).

[21] P. A. Lee, N. Nagaosa, and X.-G. Wen, Doping a Mott insulator: Physics of high-temperature superconductivity, Rev. Mod. Phys. **78**, 17 (2006).

[22] L. Ju, T. Ren, Z. Li, Z. Liu, C. Shi, Y. Liu, S. Hong, J. Wu, H. Tian, Y. Zhou *et al.*, Emergence of high-temperature superconductivity at the interface of two Mott insulators, Phys. Rev. B **105**, 024516 (2022).

[23] J. Verlage, F. Queisser, N. Szpak, J. König, P. Kratzer, and R. Schützhold, Quasi-particle propagation across semiconductor–Mott insulator interfaces, Int. J. Theor. Phys. **63**, 285 (2024).

[24] M. C. Qian, C. Y. Fong, K. Liu, W. E. Pickett, J. E. Pask, and L. H. Yang, Half-metallic digital ferromagnetic heterostructure composed of a δ-doped layer of Mn in Si, Phys. Rev. Lett. **96**, 027211 (2006).

[25] Y.-C. Lin, Y. Chen, A. Shailos, and Y. Huang, Detection of spin polarized carrier in silicon nanowire with single crystal MnSi as magnetic contacts, Nano Lett. **10**, 2281 (2010).

[26] D. Sheets, K. Lyszak, M. Jain, G. W. Fernando, I. Sochnikov, J. Franklin, J. N. Hancock, and R. M. Geilhufe, Mott insulating low thermal expansion perovskite TiF_3, Phys. Rev. B **108**, 235140 (2023).

[27] I. V. Maznichenko, A. Ernst, D. Maryenko, V. K. Dugaev, E. Y. Sherman, P. Buczek, S. S. P. Parkin, and S. Ostanin, Fragile altermagnetism and orbital disorder in Mott insulator $LaTiO_3$, Phys. Rev. Mater. **8**, 064403 (2024).

[28] A. Ohtomo and H. Hwang, A high-mobility electron gas at the $LaAlO_3/SrTiO_3$ heterointerface, Nature (London) **427**, 423 (2004).

[29] S. Thiel, G. Hammerl, A. Schmehl, C. W. Schneider, and J. Mannhart, Tunable quasi-two-dimensional electron gases in oxide heterostructures, Science **313**, 1942 (2006).

[30] R. Pentcheva and W. E. Pickett, Charge localization or itineracy at $LaAlO_3/SrTiO_3$ interfaces: Hole polarons, oxygen vacancies, and mobile electrons, Phys. Rev. B **74**, 035112 (2006).

[31] I. V. Maznichenko, S. Ostanin, D. Maryenko, V. K. Dugaev, E. Y. Sherman, P. Buczek, I. Mertig, M. Kawasaki, and A. Ernst, Emerging two-dimensional conductivity at the interface between Mott and band insulators, Phys. Rev. Lett. **132**, 216201 (2024).

[32] J. A. Santana, J. T. Krogel, S. Okamoto, and F. A. Reboredo, Electron confinement and magnetism of $(LaTiO_3)_1/(SrTiO_3)_5$ heterostructure: A diffusion quantum Monte Carlo study, J. Chem. Theory Comput. **16**, 643 (2020).

[33] H. Ishida and A. Liebsch, Origin of metallicity of $LaTiO_3/SrTiO_3$ heterostructures, Phys. Rev. B **77**, 115350 (2008).

[34] S. Okamoto and A. J. Millis, Electronic reconstruction at an interface between a Mott insulator and a band insulator, Nature (London) **428**, 630 (2004).

[35] A. Castellanos-Gomez, X. Duan, Z. Fei, H. R. Gutierrez, Y. Huang, X. Huang, J. Quereda, Q. Qian, E. Sutter, and P. Sutter, Van der Waals heterostructures, Nat. Rev. Methods Primers **2**, 58 (2022).

[36] S. Gao, S. Zhang, C. Wang, S. Yan, X. Han, X. Ji, W. Tao, J. Liu, T. Wang, S. Yuan, G. Qu, Z. Chen, Y. Zhang, J. Huang, M. Pan, S. Peng, Y. Hu, H. Li, Y. Huang, H. Zhou *et al.*, Discovery of a single-band Mott insulator in a van der Waals flat-band compound, Phys. Rev. X **13**, 041049 (2023).

[37] B. Kang, M. Kim, C. H. Park, and A. Janotti, Mott-insulator state of FeSe as a van der Waals 2D material is unveiled, Phys. Rev. Lett. **132**, 266506 (2024).

[38] Y. Jin, M. Yan, T. Kremer, E. Voloshina, and Y. Dedkov, Mott–Hubbard insulating state for the layered van der Waals $FePX_3$ (X: S, Se) as revealed by NEXAFS and resonant photoelectron spectroscopy, Sci. Rep. **12**, 735 (2022).

[39] S. Okamoto and A. J. Millis, Spatial inhomogeneity and strong correlation physics: A dynamical mean-field study of a model

Mott-insulator–band-insulator heterostructure, Phys. Rev. B **70**, 241104(R) (2004).

[40] S. Okamoto, Nonequilibrium transport and optical properties of model metal–Mott-insulator–metal heterostructures, Phys. Rev. B **76**, 035105 (2007).

[41] F. Queisser, K. V. Krutitsky, P. Navez, and R. Schützhold, Equilibration and prethermalization in the Bose-Hubbard and Fermi-Hubbard models, Phys. Rev. A **89**, 033616 (2014).

[42] P. Navez and R. Schützhold, Emergence of coherence in the Mott-insulator–superfluid quench of the Bose-Hubbard model, Phys. Rev. A **82**, 063603 (2010).

[43] F. Queisser and R. Schützhold, Boltzmann relaxation dynamics in the strongly interacting Fermi-Hubbard model, Phys. Rev. A **100**, 053617 (2019).

[44] D. P. Arovas, E. Berg, S. A. Kivelson, and S. Raghu, The Hubbard model, Annu. Rev. Condens. Matter Phys. **13**, 239 (2022).

[45] M. Qin, T. Schäfer, S. Andergassen, P. Corboz, and E. Gull, The Hubbard model: A computational perspective, Annu. Rev. Condens. Matter Phys. **13**, 275 (2022).

[46] L. D. Landau, The theory of a Fermi liquid, J. Exptl. Theoret. Phys. (U.S.S.R.) **30**, 1058 (1956) [Sov. Phys. JETP **3**, 920 (1957)].

[47] V. V. Solovyev and I. V. Kukushkin, Renormalized Landau quasiparticle dispersion revealed by photoluminescence spectra from a two-dimensional Fermi liquid at the MgZnO/ZnO heterointerface, Phys. Rev. B **96**, 115131 (2017).

[48] J. Hubbard, Electron correlations in narrow energy bands-IV. The atomic representation, Proc. R. Soc. London A **285**, 542 (1965).

[49] S. G. Ovchinnikov and V. V. Val'kov, *Hubbard Operators in the Theory of Strongly Correlated Electrons* (World Scientific, 2004).

[50] F. Mancini and A. Avella, The Hubbard model within the equations of motion approach, Adv. Phys. **53**, 537 (2004).

[51] M. Pinterić, P. Lazić, A. Pustogow, T. Ivek, M. Kuveždić, O. Milat, B. Gumhalter, M. Basletić, M. Čulo, B. Korin-Hamzić, A. Löhle, R. Hübner, M. Sanz Alonso, T. Hiramatsu, Y. Yoshida, G. Saito, M. Dressel, and S. Tomić, Anion effects on electronic structure and electrodynamic properties of the Mott insulator $\kappa-(\mathrm{BEDT-TTF})_2\mathrm{Ag}_2(\mathrm{CN})_3$, Phys. Rev. B **94**, 161105(R) (2016).

[52] S. Tomeno, M. Maesato, Y. Yoshida, A. Kiswandhi, and H. Kitagawa, Triangular-lattice organic Mott insulator with a disorder-free polyanion, Inorg. Chem. **59**, 8647 (2020).

[53] Y. Shimizu, H. Akimoto, H. Tsujii, A. Tajima, and R. Kato, Mott transition in a valence-bond solid insulator with a triangular lattice, Phys. Rev. Lett. **99**, 256403 (2007).

[54] L. M. Roth, Electron correlation in narrow energy bands. I. The two-pole approximation in a narrow *S* band, Phys. Rev. **184**, 451 (1969).

[55] A. Avella, The Hubbard model beyond the two-pole approximation: A composite operator method study, Eur. Phys. J. B **87**, 45 (2014).

[56] A. Georges, G. Kotliar, W. Krauth, and M. J. Rozenberg, Dynamical mean-field theory of strongly correlated fermion systems and the limit of infinite dimensions, Rev. Mod. Phys. **68**, 13 (1996).

[57] A. Georges and G. Kotliar, Hubbard model in infinite dimensions, Phys. Rev. B **45**, 6479 (1992).

[58] F. Queisser, C. Kohlfürst, and R. Schützhold, Back-reaction and correlation effects on prethermalization in Mott-Hubbard systems, Phys. Rev. B **109**, 195140 (2024).

[59] Z. S. Popovic and S. Satpathy, Wedge-shaped potential and Airy-function electron localization in oxide superlattices, Phys. Rev. Lett. **94**, 176805 (2005).

[60] S. Okamoto, A. J. Millis, and N. A. Spaldin, Lattice relaxation in oxide heterostructures: $\mathrm{LaTiO_3/SrTiO_3}$ superlattices, Phys. Rev. Lett. **97**, 056802 (2006).

[61] I. Leonov, V. I. Anisimov, and D. Vollhardt, Metal-insulator transition and lattice instability of paramagnetic $\mathrm{V_2O_3}$, Phys. Rev. B **91**, 195115 (2015).

[62] A. Shikin, D. Vyalikh, G. Prudnikova, and V. Adamchuk, Phase accumulation model analysis of quantum well resonances formed in ultra-thin Ag, Au films on W(1 1 0), Surf. Sci. **487**, 135 (2001).

[63] N. V. Smith, Phase analysis of image states and surface states associated with nearly-free-electron band gaps, Phys. Rev. B **32**, 3549 (1985).

[64] A. Danese and R. A. Bartynski, Phase analysis of quantum well states in metallic multilayers: Periodicity and thickness dependence of the oscillatory magnetic coupling, Phys. Rev. B **65**, 174419 (2002).

[65] M. Davy, Z. Shi, J. Wang, X. Cheng, and A. Z. Genack, Transmission eigenchannels and the densities of states of random media, Phys. Rev. Lett. **114**, 033901 (2015).